

# Realizing the Switching of Optoelectronic Memory and Ultrafast Detector in Functionalized-Black Phosphorus/MoS<sub>2</sub> Heterojunction

Chang Liu, Shuimei Ding, Qianlei Tian, Xitong Hong, Wanhan Su, Lin Tang, Liming Wang, Mingliang Zhang, Xingqiang Liu,\* Yawei Lv, Johnny C. Ho,\* Lei Liao,\* and Xuming Zou\*

A single device with switchable functions is highly attractive to the growing demands of complex optoelectronics. However, most of the currently reported devices either exhibit a lack of multifunction operation or require complex electrode configurations with limited performances. Here, a new concept of a functionalized-black phosphorus (f-BP)/MoS<sub>2</sub> heterojunction is proposed, which enables the coexistence of an optoelectronic memory and a detector in a single device. The oxidation-induced artificial-traps on the BP surface result in a gate-modulated photogating effect, so that the device can be freely switched between memory and detector by simply changing the back-gate voltage. In the memory model, the device has an ultra-long storage time (10 years), an ultra-high on/off ratio ( $3.5 \times 10^7$ ), and outstanding multi-bit storage ( $\approx 90$  states), while in the detector model, the device still exhibits a fast response (130/260  $\mu\text{s}$ ), an impressive responsivity ( $22.2 \text{ A W}^{-1}$ ), and self-driven broadband detection (ultraviolet to near-infrared). Most importantly, the highly anisotropic BP enables fast NIR polarization resolution with a maximum polarization ratio of 6.98 at 1064 nm.

## 1. Introduction

As mono-function optoelectronic devices continue to mature and approach their fundamental limit, a burning question is how to develop technology enabled with reduced product size and increasing functionality.<sup>[1,2]</sup> For now, monolithic optoelectronic technologies that integrate two or more mono-function components into a single chip can advance inspiring and promising applications, which further fill the needs of emerging industries such as unmanned technology and artificial intelligence.<sup>[3–5]</sup> For example, the artificial visual system generally combines a sensitive photodetector to perceive the multiple visual inputs, a memory unit to store the visual information, and a processing unit to conduct complex image-processing tasks.<sup>[6]</sup> Although


these mono-function integrations enable improvement in device performance and functionality, the manufacturing of a variety of components and then assembling them into a chip inevitably complicates the fabrication process and increases the cost.<sup>[7,8]</sup> Therefore, it is highly desirable to achieve individual multifunctional components, which is beneficial for simplifying the fabrication process, boosting the integration level, and expanding the application fields.

Two-dimensional (2D) materials provide a unique opportunity for the development of artificial heterojunction due to weak van der Waals (vdW) forces between individual layers.<sup>[9–13]</sup> To date, various vdW heterojunctions formed by vertical stacking 2D materials have enabled a variety of functions and applications, including p-n junction,<sup>[9]</sup> tunneling transistors,<sup>[14]</sup> tunable inverter,<sup>[2]</sup> photodetectors,<sup>[15]</sup> light-emitting diodes,<sup>[16]</sup> and non-volatile memories,<sup>[17]</sup> et al. However, for different functions, people usually consider the conductivity type and band-structure of these materials, then design different 2D heterojunction architectures to achieve. In this case, a single heterojunction with switchable functions is highly important. Although a few multifunctional heterojunctions have been reported,<sup>[2,7,8]</sup> they still require complex electrode deposition and different test ports to accomplish functional switching, which is not inherently a

C. Liu, S. Ding, Q. Tian, X. Hong, W. Su, L. Tang, L. Wang, M. Zhang, X. Liu, Y. Lv, L. Liao, X. Zou  
Key Laboratory for Micro/Nano Optoelectronic Devices of Ministry of Education & Hunan Provincial Key Laboratory of Low-Dimensional Structural Physics and Devices, School of Physics and Electronics  
Hunan University  
Changsha 410082, China  
E-mail: liuxq@hnu.edu.cn; liaolei@whu.edu.cn; zouxuming@hnu.edu.cn

C. Liu, X. Liu, Y. Lv, L. Liao, X. Zou  
College of Semiconductors (Integrated Circuits)  
Hunan University  
Changsha 410082, China

J. C. Ho  
Department of Materials Science and Engineering  
City University of Hong Kong  
Hong Kong SAR 999077, China  
E-mail: johnnyho@cityu.edu.hk

 The ORCID identification number(s) for the author(s) of this article can be found under <https://doi.org/10.1002/lpor.202200486>

DOI: 10.1002/lpor.202200486

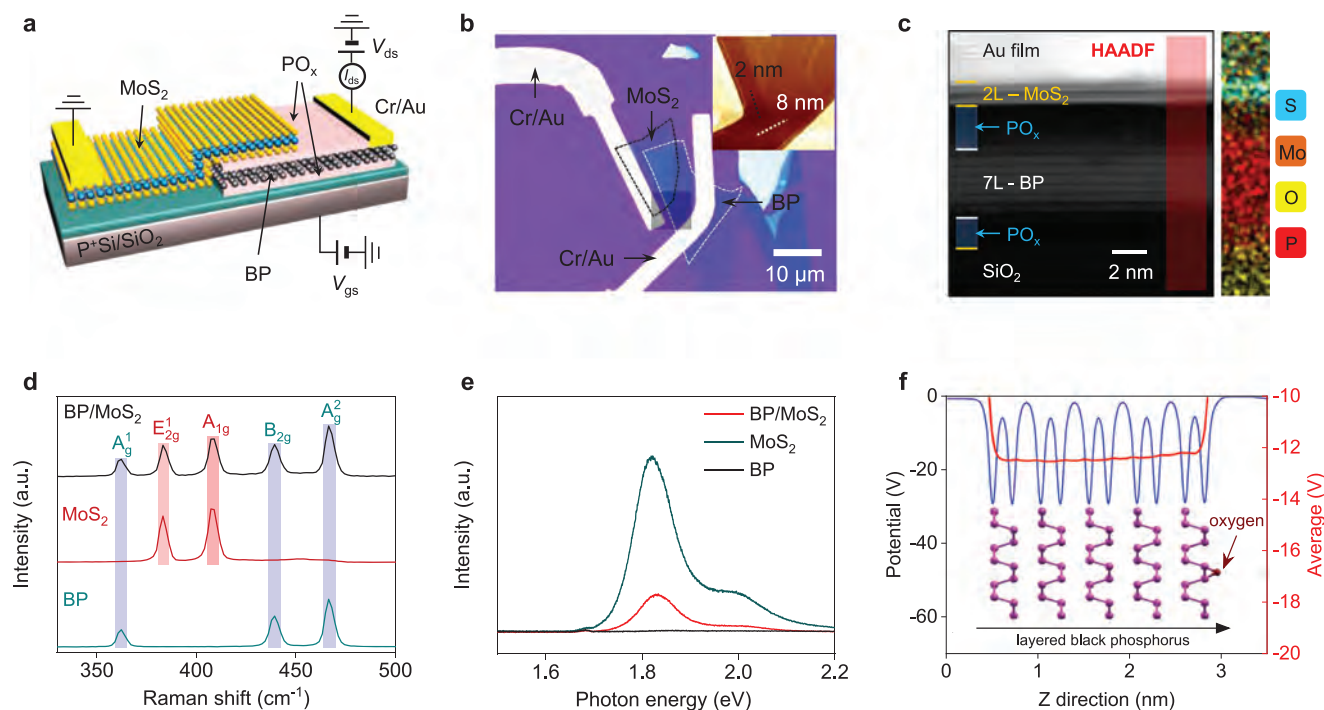


**Figure 1.** Structure schematics and material characterizations of the f-BP/MoS<sub>2</sub> heterojunction. a) Schematic diagram of the device configuration. b) Optical microscopic images of the device. Inset: AFM image of the corresponding area. c) Cross-sectional STEM image and the corresponding EDS element distribution mapping. d) Raman spectra of BP and MoS<sub>2</sub> and their heterojunction. e) PL measurement of BP and MoS<sub>2</sub> and their heterojunction. f) The potential value of layered BP after oxygen adsorption.

multifunctional integrated stand-alone device. Additionally, their functions mainly focus on the traditional electrical-functions such as diode, transistor, inverter, rectifier, etc. There are no reported devices with switchable optoelectronic functions. In terms of performance, most reported devices achieve multifunctional operation at the expense of device performance. Such as, an asymmetric 2D heterojunction was recently reported to function as transistor, rectifier, and photodetector,<sup>[1]</sup> whose multifunctional operation is achieved by stacking four 2D materials, including Graphene, BN, MoS<sub>2</sub>, and MoTe<sub>2</sub>. As we know, the stacking of multiple 2D materials can facilitate multifunctional operations. However, this strategy results in serious current jitter and large noise originating from the scattering of different materials.<sup>[18]</sup> Also, the multiple material-transfers not only complicate the fabrication process but introduce more impurities to degrade device performance. Therefore, designing high-performance and multifunctional heterojunction devices remains a challenge.

Here, we demonstrate a new concept of 2D defect-engineering heterojunction to realize gate-controlled optoelectronic memory and photodetector switching in a single device. Although interface defects are often considered problematic, defect-engineering has proven to be a simplistic way to modulate properties and create new functions in contemporary materials science.<sup>[19–22]</sup> In our work, the freely switching capability is achieved by black phosphorus (BP) oxidation-induced surface defects in a planar BP/MoS<sub>2</sub> heterojunction, in which the trapped holes can induce a gate-voltage-controlled photogating effect for optoelectronic memory and detector operation. At negative gate voltage ( $V_{gs} = -60$  V), when a laser pulse is applied, the photo-generated

carriers in heterojunction are spatially separated by a large built-in potential. The type-II heterojunction allows electrons rapidly transfer from BP to MoS<sub>2</sub>, while leaving the trapped holes to induce a high photogain as electron recirculates in the channel. In this case, our device is operated as an optoelectronic memory with ultra-low dark current (0.13 pA), ultra-high switching ratio ( $3.5 \times 10^7$ ), outstanding multi-bit storage (90 states) as well as excellent broadband memory from ultraviolet to near-infrared (UV to NIR). Under a positive gate voltage ( $V_{gs} = +20$  V), the Fermi level of the BP layer is shifted upward and a large number of electrons are able to neutralize the trapped holes, thus attenuating the photogating effect and transforming the device into a detector that quickly responds to optical signals. As a result, the device exhibits fast response (130/260  $\mu$ s), stable photoswitching (750 cycles), self-driven broadband detection (375–1550 nm), and infrared polarization resolution (a maximum polarization ratio of 6.98). All these results obtained in our multifunction heterojunction are already much better in nearly all aspects of performance than the previously reported 2D mono-function memories and detectors, achieving the optimal balance between all figure-of-merits.

## 2. Results

### 2.1. Device Structure and Basic Characterizations

**Figure 1a** gives a schematic diagram of our multifunction heterojunction device. The device architecture is a 2D planar heterojunction consisting of a BP layer at the bottom and a MoS<sub>2</sub>

layer at the top, in which two self-assembled phosphorus oxide ( $\text{PO}_x$ ) layers are located on the upper and lower surfaces of BP. The Cr/Au (10/50 nm) electrode contacts on each layer and a gate voltage ( $V_{\text{gs}}$ ) applied to the  $\text{P}^+\text{Si}$  substrate adjusts the carrier densities in each semiconductor layer. The straightforward preparation steps are schematically illustrated in Figure S1, Supporting Information. Figure 1b shows the optical image of a representative fabricated device. The inset is the atomic force microscopy (AFM) image of the selected region, and the thickness information of two materials is shown in Figure S2, Supporting Information, where the BP and  $\text{MoS}_2$  is 8 and 3 nm, respectively. The  $\text{PO}_x$  layer plays an important role in the function switching of our device, which can be seen in cross-sectional scanning transmission electron microscopy (STEM) images. As shown in Figure 1c, two obvious  $\text{PO}_x$  layers can be observed at the BP/ $\text{MoS}_2$  and BP/ $\text{SiO}_2$  interface. The related O and P elements can be further confirmed by energy-dispersive X-ray spectroscopy (EDS) element distribution mapping. We also note that the thicknesses of  $\text{MoS}_2$  and BP in the heterojunction are 2 and 7 layers, respectively. This thickness can maintain high light adsorption efficiency while providing high carrier mobility and large switching ratio for transistor operation. The intensity of all elements in heterojunction is demonstrated in Figure S3, Supporting Information, where the element distribution is consistent with the ideal device architecture we designed. The crystalline quality of BP,  $\text{MoS}_2$ , and heterojunction is further tested by Raman characterization (Figure 1d). Three strong peaks of BP can be seen at 362, 439, and 466  $\text{cm}^{-1}$ , representing the  $\text{A}_g^1$ ,  $\text{B}_{2g}$ , and  $\text{A}_g^2$  modes, respectively.<sup>[23,24]</sup> For  $\text{MoS}_2$ , the peaks are located at 383 and 407  $\text{cm}^{-1}$ , corresponding to the in-plane vibration mode  $\text{E}_{2g}^1$  and out-of-plane vibration mode  $\text{A}_{1g}$ , respectively.<sup>[23]</sup> For their heterojunction, the spectra contain all the peaks of  $\text{MoS}_2$  and BP. There is no peak shift or degradation, indicating the heterojunction is coupled strongly with a high crystalline quality. Figure 1e gives the photoluminescence (PL) of  $\text{MoS}_2$ , BP, and their heterojunction. Here, a significant PL quenching can be observed in the heterojunction region. The peak intensity decreases by 79% compared to the pristine  $\text{MoS}_2$  material due to the exciton dissociation and interlayer charge transfer in hetero-interface.<sup>[25]</sup> This result also demonstrates that the presented BP/ $\text{MoS}_2$  heterojunction has a type-II band alignment as previous studies,<sup>[23–29]</sup> which enables ultra-efficient carrier transfer. In order to verify the trapping effect of oxidized BP layer for holes, we calculated the potential of layered BP along the thickness direction after oxygen adsorption by density function theory (DFT) (Figure 1f). The results show that the average potential (red curve) increases obviously towards the oxygen-adsorbed BP surface, verifying that the oxidation-induced traps can effectively confine holes.

## 2.2. Gate-Controlled Photoresponse Characteristics and Mechanisms

To probe the different operation models, we systemically study the gate-controlled photoresponse characteristics of functionalized-BP (f-BP)/ $\text{MoS}_2$  heterojunction. Figure 2a demonstrates the transfer curves ( $I_{\text{ds}} - V_{\text{gs}}$ ) in dark and light states with a fixed drain-source voltage ( $V_{\text{ds}}$ ) of  $-2$  V. In this device configuration, the source-drain electrodes are in contact with

$\text{MoS}_2$  and BP layer, while leaving the overlapped region away from the electrodes to form a lateral heterojunction field-effect transistor (FET).<sup>[2]</sup> In this case, electrons are injected from the source to drain electrode through the functionalized-BP channel, BP/ $\text{MoS}_2$ / $\text{PO}_x$  hetero-interface and  $\text{MoS}_2$  channel, consecutively. The back-gate controls the entire channel electrostatic potential, resulting in non-monotonic current modulation. Therefore, in the dark state, the  $I_{\text{ds}} - V_{\text{gs}}$  curves of heterojunction exhibit an N-shaped curve, where two threshold voltages ( $V_{\text{th}}$ ) located at  $-60$  and  $20$  V can be found. Here, threshold voltage is defined as the inflection point of the transfer curve in dark. This characteristic can be further confirmed by the transfer characteristics of n-type  $\text{MoS}_2$  and p-type BP (Figure S4, Supporting Information), revealing the electrical properties of heterojunction can be modulated by  $\text{MoS}_2$  and BP individually. For the first threshold voltage ( $V_{\text{th}}^1 = -60$  V), the  $\text{MoS}_2$  channel is fully depleted with a sufficiently negative gate bias, which can turn off the entire channel and results in an ultra-low dark current ( $I_{\text{dark}}$ ) of  $\approx 1.2 \times 10^{-13}$  A. While at the second threshold voltage ( $V_{\text{th}}^2 = 20$  V), the device current is dominated by the non-overlapped BP channel, in which the BP channel is completely depleted, so the current is again decreased to  $\approx 8.3 \times 10^{-10}$  A. It is worth noting that the functionalized BP does not affect the basic electrical properties of p-n junction, whose output curve ( $I_{\text{ds}} - V_{\text{ds}}$ ) still exhibits excellent rectification characteristics (Figure S5, Supporting Information). Under light illumination, when we used a 532 nm laser with an incident power density ( $P_{\text{light}}$ ) of  $3.6 \text{ W cm}^{-2}$ , the heterojunction is fully turned on, resulting in a large on/off ratio especially at the positions of  $V_{\text{th}}^1$  and  $V_{\text{th}}^2$ . With these characteristics in mind, we further explored the transfer characteristic under different  $P_{\text{light}}$  from 0.08 to  $3600 \text{ mW cm}^{-2}$  (Figure S6, Supporting Information). When we used an ultra-low  $P_{\text{light}}$  of  $80 \mu\text{W cm}^{-2}$ , an obvious  $V_{\text{th}}^1$  shift toward the negative direction can be observed, while this shift is small at  $V_{\text{th}}^2$ . Considering the dominated n-type  $\text{MoS}_2$  channel, this shift can be attributed to the trapping of photo-generated holes in  $\text{PO}_x$  layer, indicating a profound photogating effect obtained here.<sup>[17,30]</sup> Meanwhile, the ratios of light-state current ( $I_{\text{light}}$ ) to dark-state current ( $I_{\text{dark}}$ ) at  $V_{\text{th}}^1$  and  $V_{\text{th}}^2$  are extracted in Figure 2b. Our device shows an ultra-high on/off ratio of  $3.5 \times 10^7$  at  $V_{\text{th}}^1$ , while the value can still reach  $2.6 \times 10^3$  at  $V_{\text{th}}^2$ . Such a high value can be attributed to the ultra-low dark current and the amplified output current caused by photogating effect.<sup>[30]</sup> To confirm this photoresponse mechanism, we extracted the photocurrent ( $I_{\text{ph}} = I_{\text{light}} - I_{\text{dark}}$ ) of  $V_{\text{th}}^1$  and  $V_{\text{th}}^2$  as a function of  $P_{\text{light}}$ , which is fitted according to the equation of  $I_{\text{ph}} \propto P_{\text{light}}^\alpha$ . Here,  $\alpha$  is a constant. Generally,  $\alpha = 1$  represents a perfect photoconductive effect, and  $\alpha < 1$  represents the existence of a photogating effect.<sup>[31]</sup> In both  $V_{\text{th}}^1$  ( $-60$  V) and  $V_{\text{th}}^2$  ( $20$  V), the fitted  $\alpha$  values are less than 1, which fully indicates the presence of photogating effect in our device (Figure 2c). We also observe that the value of  $V_{\text{th}}^1$  (0.24) is smaller than  $V_{\text{th}}^2$  (0.66). This result reveals that a stronger photogating effect appears at  $V_{\text{th}}^1$ , which is consistent with its larger threshold shift.

To fully explore the gate-controlled function switching, we conducted time-dependent photoresponse measurements at different gate voltages (Figure 2d). Here, a 532 nm laser pulse (power density is  $675 \text{ mW cm}^{-2}$  and duration time is 5 s) is applied as the incident light signal. When the  $V_{\text{gs}}$  is fixed at  $V_{\text{th}}^1$  ( $-60$  V), the



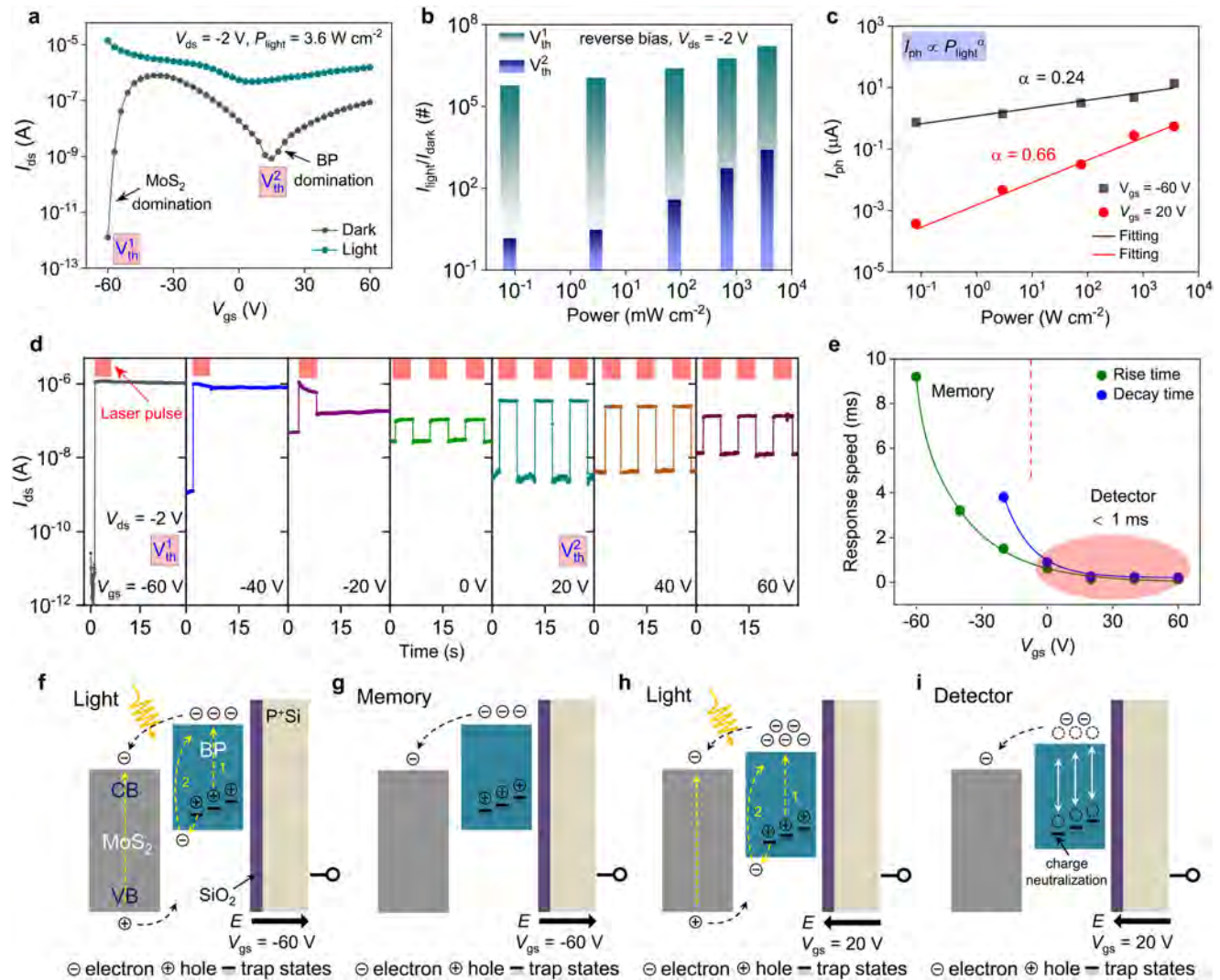


**Figure 2.** Gate-controlled photoresponse characteristics and mechanisms. a)  $I_{ds}$ - $V_{gs}$  curves of f-BP/MoS<sub>2</sub> heterojunction in the dark and light state at  $V_{ds} = -2$  V. b) The extracted  $I_{light}/I_{dark}$  values with different laser power density. c) The photocurrent plotted as a function of laser power densities. d) Photoresponse characteristics under different gate voltages. e) The extracted response speed under different gate voltages. f–i) Mechanisms of the device in memory mode ( $V_{gs} = -60$  V) with (f) and without (g) light irradiation, respectively; in detector mode ( $V_{gs} = 20$  V) with (h) and without (i) light irradiation, respectively. Here, VB and CB denote the energy level of valence band and conduction band, respectively, and the “E” arrow denotes the gate electric field direction.

device has an ultra-low dark current of  $\approx 1.2 \times 10^{-13}$  A due to the transistor being turned off. The applied laser pulse can quickly raise the device current to saturation value ( $I^{on}$ ) and then maintain a stable non-decaying state. In other words, the input optical signal can be efficiently converted to current and stored. This can be explained as follows: the incident photons can excite a large number of electron-hole pairs, which can be separated by the interface electric field of heterojunction. When photo-generated electrons are transferred in the heterojunction, the holes are still trapped on the surface of BP. Under a large negative gate voltage, the trapped holes are difficult to escape for charge neutralization, and then induce a strong photogating effect to further amplify the photocurrent. Thus, the device can maintain a persistent photoconductive (PPC) state. Considering this characteristic, the device at  $V_{th}^1$  can function as a nonvolatile optoelectronic memory,

where the optical signal can be written, stored, and readout.<sup>[32]</sup> Here, the PPC behavior is dependent on the ozone treatment time (Figure S7, Supporting Information). The 60 s treatment time exhibits the strongest PPC behavior in which the long-live charge traps can govern the electron-hole recombination, while the devices without ozone treatment showed almost no PPC behavior. With the increasing gate bias (−40 and −20 V), the dark current increases which is consistent with the transfer curve of the device in the dark state. At  $V_{gs} \geq 0$  V, the PPC behavior disappears and the device exhibits a fast photoswitching response like a typical reverse-biased photodiode. This is due to a large number of electrons generated in the p-type BP layer at a positive  $V_{gs}$ , which can neutralize the trapped photo-generated holes and weak the photogating effect. In this case, the device can function as a photodetector with an ultrafast photoresponse switching. We can

observe that the device has the largest on/off ratio at  $V_{th}^2$  ( $V_{gs} = 20$  V), which originates from the low dark current here. Note that the dark current at  $V_{th}^2$  is mainly controlled by the p-type BP according to the heterojunction transfer curve, which is obviously higher than that of  $V_{th}^1$ . Although a lower dark current can reduce power consumption and increase the sensitivity of photodetector, this dark current is already one order of magnitude lower than the lowest value reported for MoS<sub>2</sub>/BP heterojunction FET,<sup>[2]</sup> which is a record value. When we choose a thicker BP ( $\approx 12$  nm) for the heterojunction, there is a higher dark current of  $3.8 \times 10^7$  A (Figure S8, Supporting Information). Theoretically, thinner BP layers are capable of having lower off-state currents. However, our device configuration requires the BP to have strong light absorption even after the oxidation treatment. After extensive exploration, we finally found that  $\approx 8$  nm BP is the optimal thickness, which ensures the optimal balance of all device performances. Additionally, the response speed at different gate voltages is also tested by the oscilloscope (Figure S9, Supporting Information). In our f-BP/MoS<sub>2</sub> heterojunction, the photo-generated carrier separation and recombination are controlled by the reversed-bias p-n junction, where this process is known to be faster than other carrier separation and recombination processes. Therefore, the rise and decay times for two models are much faster than the conventional optoelectronic memory and detector as shown in Figure 2e. We also notice that the detector mode is significantly faster than the memory, which is attributed to the weaker trap-assisted carrier separation and recombination as described above. This result also justifies the feasibility of operating our device as an ultrafast detector.

To better understand the mechanisms of multifunctional operations, we plotted the schematic band diagrams of the heterojunction in four different operational states. For the memory model (at  $V_{gs} = -60$  V), electron-hole pairs are generated in both MoS<sub>2</sub> and BP layers with light irradiation (Figure 2f). Here, the functionalized-BP layer is used as the dominant adsorption layer due to its thicker thickness as well as narrower-bandgap,<sup>[2]</sup> in which the oxygen-induced impurity energy-levels have two possible ways to excite electrons: 1) direct excitation by absorbing photon energy in the light; 2) the valence band electrons related to the trapped holes are excited to conduct band. In this case, when a large number of electrons are transferred from the BP to the MoS<sub>2</sub> layer under the built-in potential, the holes are confined in the BP surface, leading to a high photogain given by the formal of  $\tau_{lifetime}/\tau_{transit}$ ,<sup>[26,30]</sup> where  $\tau_{lifetime}$  denotes the lifetime of trapped holes in BP and  $\tau_{transit}$  denotes the transit time for the electrons transporting in the conducting channel. The trapped-holes can rapidly raise the Fermi energy level of BP, providing a photogating effect with the recirculation of electrons in the channel.<sup>[17]</sup> Thus, the BP acts not only as a light-absorbing layer but also as an electron-injecting “valve”, and the incident photon acts as the trigger for the switch.<sup>[33]</sup> When the light irradiation stops (Figure 2g), the low electron concentration in BP is unable to neutralize the trapped holes. The trapped-holes induced strong photogating effect makes the device in a stable PPC state and the device can be operated as a nonvolatile optoelectronic memory. In contrast, when a gate voltage of +20 V is applied, the Fermi energy level of BP shifts upward. Under light irradiation, electron-hole pairs are still generated and transferred as in the memory mode (Figure 2h). But after the light irradiation stops (Figure 2i),

a large number of electrons in BP is able to neutralize the trapped holes, thus attenuating the photogating effect and increasing the barrier height of the heterojunction. As a result, the PPC behavior disappears and the device works like a photodiode to achieve fast photoresponse switching.

### 2.3. Multi-Bit Optoelectronic Memory Model

Nonvolatile optoelectronic memories, as it allows multi-bit storage operations by optical writing and electrical readout, are an important component in the modern electronic industry. When we fix the gate voltage at  $V_{th}^1$  ( $-60$  V), our device can switch to a nonvolatile optoelectronic memory model. In Figure 3, we systematically investigated the optoelectronic properties of f-BP/MoS<sub>2</sub> memory, especially in storage time and multi-bit storage. Specifically, Figure 3a shows the photo-response  $I_{ds}$ - $V_{ds}$  curves of the device under 532 nm laser illumination at  $V_{gs} = -60$  V and  $V_{ds} = -2$  V. In dark, the device has an ultra-low dark current of 0.12 pA due to the complete depletion of MoS<sub>2</sub> layer and large electron injection barrier. This dark current value is 8, 33, 39, and 48 times lower than the reported WSe<sub>2</sub>/BN memory,<sup>[32]</sup> monolayer MoS<sub>2</sub> artificial traps memory,<sup>[34]</sup> MoS<sub>2</sub>/PVP/Au practical memory,<sup>[35]</sup> and MoS<sub>2</sub>/Al<sub>2</sub>O<sub>3</sub>/Graphene memory,<sup>[36]</sup> respectively. Under the laser illumination, even at an ultra-low power density of 60.4 nW cm<sup>-2</sup>, our device still has a significant current increase of nearly four orders of magnitude. The extracted  $I_{light}/I_{dark}$  values are shown in Figure S10, Supporting Information, which is an important parameter that determines the storage capacity of the optoelectronic memory. Our device exhibits a maximum  $I_{light}/I_{dark}$  value of  $3.5 \times 10^7$  at  $V_{ds} = -2$  V and  $P_{light} = 3.6$  W cm<sup>-2</sup>. This value is 4 and 1 orders of magnitude higher than those reported defective engineered MoS<sub>2</sub> memory<sup>[34]</sup> and MoS<sub>2</sub>/h-BN/Graphene memory,<sup>[37]</sup> respectively. Such a high switching ratio is due to ultra-low dark current, ultra-high co-adsorption efficiency, and current amplification by a strong photogating effect. We can also observe an obvious photovoltaic (PV) effect in strong light. To quantify this PV effect, we extracted the photocurrent as a function of  $V_{ds}$  and  $P_{light}$  plotted in a contour graph (Figure 3b). With the increasing laser power, the photocurrent keeps on increasing, where a high short-circuit current ( $I_{sc}$ ) of  $1.1 \times 10^{-7}$  A and a large open-circuit voltage ( $V_{oc}$ ) of 0.3 V are obtained (Figure S11a, Supporting Information). Also, the external quantum efficiency (EQE) at  $V_{gs} = -60$  V can be further evaluated by the formula of  $EQE = I_{sc} \cdot h \cdot c / P_{in} \cdot e \cdot \lambda$ , where  $h$ ,  $c$ ,  $P_{in}$ ,  $e$ , and  $\lambda$  are the Planck constant, the speed of light, the incident optical power, the charge of single electron, and the wavelength of incident laser, respectively.<sup>[18]</sup> Here, the maximum EQE value is calculated to be  $\approx 27.4\%$  at  $P_{light} = 80$   $\mu$ W cm<sup>-2</sup> (Figure S11b, Supporting Information). This strong PV effect makes our optoelectronic memory different from other memory, which may allow our memory to finish the full power-off storage while maintaining a high secondary read-current (as demonstrated by the blue line of Figure 3d). In addition, the switching ratio, responsivity ( $R$ ) is an important parameter to quantitatively assess the photocurrent generated on the active area of the device. The  $R$  is given by the formula of  $R = I_{ph}/P_{light} \cdot S$ , where  $S$  refers to the overlapping area of the heterojunction.<sup>[17]</sup> As shown in Figure 3c, the  $R$  can be modulated by the varying  $V_{ds}$  and  $P_{light}$ . It is observed that the  $R$  in

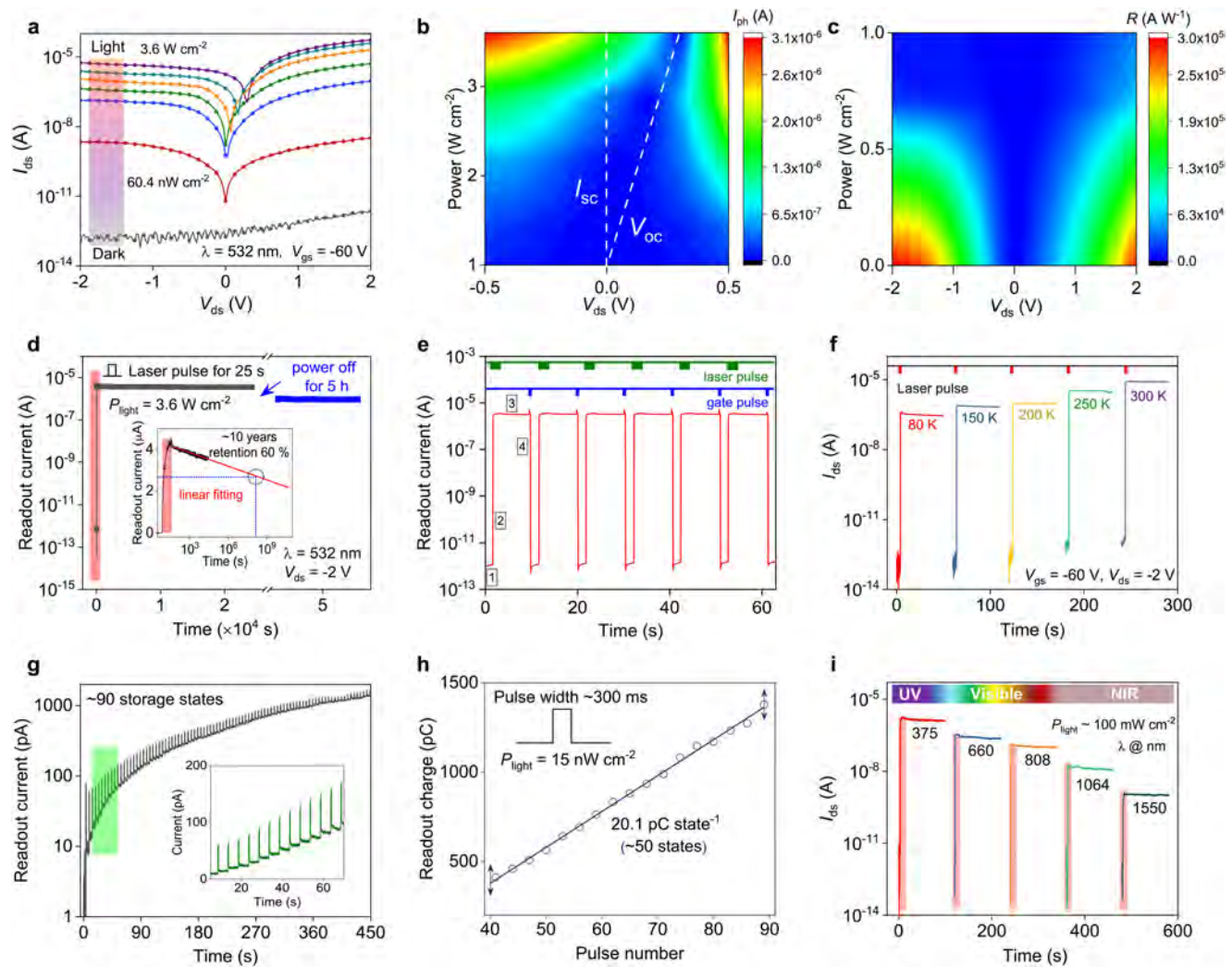


**Figure 3.** Optoelectronic storage performances in memory mode. a)  $I_{ds}$ - $V_{ds}$  curves of the device under 532 nm laser illumination at  $V_{gs} = -60$  V. b)  $V_{ds}$  and  $P_{light}$  dependent photocurrent to show the  $V_{oc}$  and  $I_{sc}$  of our device. c)  $V_{ds}$  and  $P_{light}$  dependent responsivity extracted from the  $I_{ds}$ - $V_{ds}$  curves. d) Long-term storage tests written by a 532 nm laser pulse with  $P_{light}$  of  $3.6 \text{ W cm}^{-2}$  for 25 s. Inset: estimated storage time and efficiency according to current decay trend. e) Writing and erasing operation of the memory using laser and gate voltage pulses, respectively. f) PPC characteristics at different temperatures (80–300 K). Here, the applied laser pulser is 532 nm ( $3.6 \text{ W cm}^{-2}$  for 2 s). g) Dynamic behavior of the memory under the repeated laser pulses (duration: 300 ms,  $P_{light} = 15 \text{ nW cm}^{-2}$ ). h) The linear fitting of the readout current in (g). i) The broadband memory characteristics written by different wavelength lasers ranging from UV to NIR (375–1550 nm). Here, the laser duration is set to 10 s.

negative bias is generally greater than the forward, which may be caused by the lower dark current in the reversed-bias state. Also, the  $R$  decreases with the laser power density, which can be explained by the high recombination rate of photo-generated carriers at strong laser illumination. Here, our device exhibits a maximum  $R$  value of  $3.0 \times 10^5 \text{ A W}^{-1}$  at  $V_{ds} = -2$  V, which is much higher than most 2D optoelectronic memories.<sup>[34,37,38]</sup> Next, we focus on storage time testing, which is an important parameter for practical applications. When the device is illuminated by a strong 532 nm laser for 25 s ( $P_{light} = 3.6 \text{ W cm}^{-2}$ ), the readout current raises rapidly to the  $I^{on}$  of  $3.0 \times 10^{-6}$  A (Figure 3d). As the laser is turned off, the  $I^{on}$  can be fully maintained with a measurement range of  $\approx 2.5 \times 10^4$  s. The storage efficiency of the device can reach 77.8 % for  $2.5 \times 10^4$  s after the end of the laser pulse (Figure S12, Supporting Information). Even after a 5-h full

power-off, that is, the bias and gate voltages are removed, a high current of  $1.1 \times 10^{-6}$  A can be secondarily readout and maintained again for  $1.5 \times 10^4$  s due to the strong PV effect. With conservative extrapolation, the readout current of the device can still be preserved at 60% for 10 years, demonstrating its potential as a non-volatile memory (Inset of Figure 3d). These results were found to be superior to all 2D heterojunction memories after systematic comparison (Figure 4a,b). The writing/erasing operations of our memory are shown in Figure 3e, which contains four basic steps, 1) OFF-state current reading, 2) laser pulse writing, 3) ON-state current reading, and 4) gate voltage pulse erasing. To be specific, when a negative gate voltage ( $-60$  V) is applied to the device, the device is in the OFF-state with an ultra-low reading current of 0.12 pA. With the laser turned on ( $3.6 \text{ W cm}^{-2}$  for 2 s), the device current instantaneously increases to  $4.2 \times 10^{-6}$  A



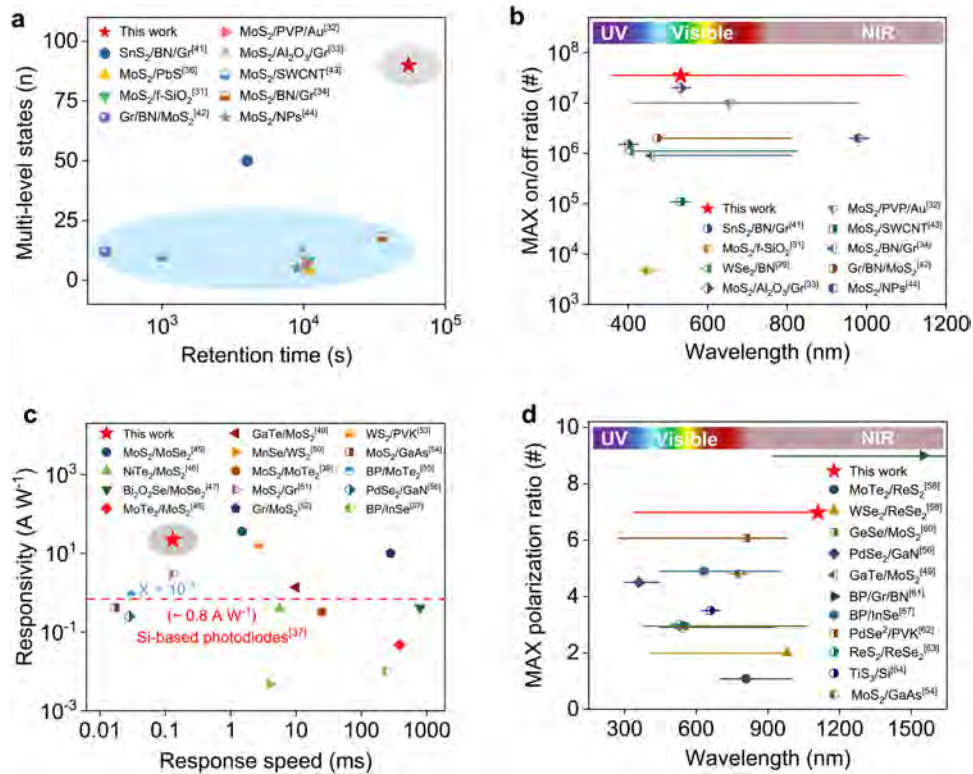


**Figure 4.** Performances comparison of our multifunction device with previously reported 2D heterojunction-based mono-function memories and detectors. For optoelectronic memories, a) the comparative retention time and number of multi-bit storage states; b) the comparative photoresponse wavelength range and maximum switching ratio. For photodetectors, c) the comparative response speed and responsivity; d) the comparative photoresponse wavelength range and maximum polarization photocurrent ratio.

with an ultra-high switching ratio of  $3.5 \times 10^7$ . When a large positive gate voltage pulse (+80 V, 300 ms) is applied to the device, the device current suddenly increases due to the back-gate capacitance effect, which can instantaneously increase the electron density. Therefore, we can see an immediate rise of  $I_{ds}$ -current, and then decreases to the initial non-conducting state, completing a writing/erasing cycle. The specific working principle is explained as follows, in the dark state, the device is operated in the OFF-state by a -60 V gate voltage. For the writing process, strong light-induced photo-generated holes are trapped in the surface of BP to keep the device in a highly conductive state. With the laser off, the long-lived charge traps effectively prevent electron-hole recombination, which results in a stable PPC state. For the erasing process, when a large positive gate voltage is applied, the BP is converted to n-type and the excess electrons are able to neutralize all the trapped-holes, causing the device to return to the initial OFF-state. To further explore the temperature stability of oxidation-induced artificial traps, PPC behaviors at varying temperatures ( $T$ ) from 80 to 300 K were tested (Figure 3f). When the device is written by laser pulses, the readout current exhibits a rapid rise at all temperatures. With the increasing temperature from 80 to 300 K, two important features can be seen: I) The PPC behaviors are not affected by temperature, suggesting that the trapped-holes can effectively resist thermal fluctuations; II) Both OFF- and ON-state currents increase with increasing temperature, which may stem from the additional current contribution of thermally excited-electrons.<sup>[39]</sup> In addition, our device shows a

maximum switching ratio at 300 K (Figure S13, Supporting Information), indicating its potential as a high-performance room temperature memory.

High-capacity multi-bit memory can avoid the complex integration of continuous scaling to ensure more memory cells per unit area. The ultra-low dark current and high photogain of our memory enable us to obtain a record multi-bit storage as shown in Figure 3g. Here, we show the dynamic behavior of our memory under periodic exposures of laser pulse ( $15 \text{ nW cm}^{-2}$ , 300 ms). The inset is an enlarged data region. Obviously, the readout current gradually increases with the number of pulses, which indicates that more holes are trapped leading to more electrons circulating in the channel. Our memory allows 90 effective storage states before current saturation. This number is an order of magnitude higher than that of previously reported optoelectronic memories (Figure 4a). To probe the practicality of the device for multi-bit storage, we further analyzed the linear characteristics of readout current (Figure 3h). Our devices can obtain up to 50 linear storage states, which steadily increased by 20.1 pA with each laser pulse applied, showing a good linearity. This also confirms that the multi-bit memory is reliable and reproducible in the case of repeated switching. Although the above performances are mainly based on a 532 nm laser, the device also has an excellent capacity for broadband storage. With varying wavelength laser from 375 to 1550 nm, the device has a perfect memory behavior under all conditions (Figure 3i). Meanwhile, the readout ON-state current is demonstrated in Figure S14, Supporting

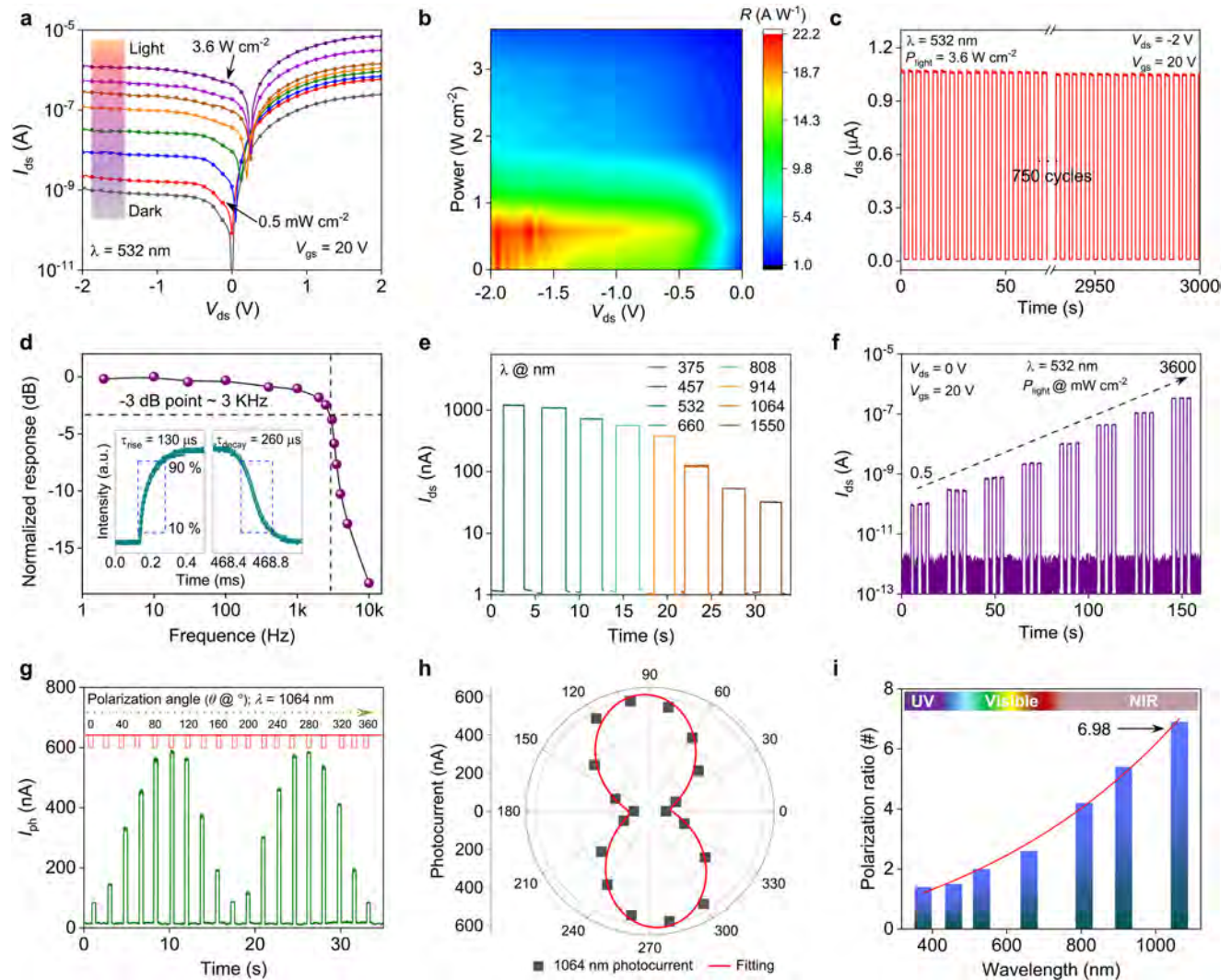


**Figure 5.** Ultrafast detection and polarization resolution in photodetector model. a)  $I_{ds}$ - $V_{ds}$  curves of the device under 532 nm laser illumination at  $V_{gs} = 20$  V. b)  $V_{ds}$  and  $P_{light}$  dependent responsivity extracted from the  $I_{ds}$ - $V_{ds}$  curves. c) Photoswitching response of the detector under 532 nm laser illumination with  $P_{light} = 16$  W  $cm^{-2}$ . d) Frequency response showing a 3 dB frequency of 3 KHz at  $\lambda = 532$  nm. Inset: the rise and decay times tested by Oscilloscope. e) Fast detection characteristics under different wavelength lasers ranging from UV to NIR (375–1550 nm). f) The self-driven detection at different  $P_{light}$ . g) Photoswitching response using laser pulses of 1064 nm and continuously changing the polarization direction. h) The extracted photocurrent as a function of polarization angle. i) The extracted polarization ratio of various wavelengths ranging from UV to NIR (375–1064 nm).

Information, which decreases gradually with increasing wavelength. It is also noted that the 375 nm laser shows the highest readout current due to the higher photon energy and co-absorption of the heterojunction. Our broadband memory is capable of storing encrypted information through different wavelength writing. Based on the optical anisotropy of the BP, we further performed polarization-resolved storage tests (Figure S15, Supporting Information). Here, we define the polarization angle ( $\theta$ ) as the angle between the polarization-light and the BP zigzag direction (e.g.,  $\theta = 0^\circ$  means that the polarization light is aligned with the zigzag direction of BP), then change the  $\theta$  to test the photocurrent of the device. When we change the  $\theta$  from 0 to 180°, we find that the device is able to store different photocurrents at different angles (Figure S15a, Supporting Information). The readout currents are further extracted and fitted in a polar co-

ordinate system (Figure S15b, Supporting Information), and we find a perfect “8” shape of the photocurrent as the angle changes, exhibiting a full-angle polarization identification.

#### 2.4. Ultrafast Photodetector Model

Photodetector is an indispensable component in many optoelectronic applications including freespace communication, remote control, medical imaging, etc. When we change the  $V_{gs}$  from  $-60$  ( $V_{th}^1$ ) to 20 V ( $V_{th}^2$ ), the device can quickly switch from a memory to a photodetector, and its performances are further explored in Figure 5. First, the  $I_{ds} - V_{ds}$  curves at  $V_{gs} = 20$  V under 532 nm laser illumination are demonstrated (Figure 5a). Even at a low power density of 0.5 mW  $cm^{-2}$ , the device still has a significant



current increase. The extracted switching ratio is shown in Figure S16, Supporting Information, where the device can obtain the largest ratio of  $1.2 \times 10^3$  at  $V_{ds} = -2$  V due to the lower dark current in reversed-bias state ( $V_{ds} < 0$  V). To quantify the photoresponse performance, the  $R$  as a function of  $V_{gs}$  and  $P_{light}$  is calculated and displayed in Figure 5b. Here, the maximum  $R$ -value can reach  $22.2$  A  $W^{-1}$ , which is one to three orders of magnitude higher than most 2D heterojunction photodetectors and commercial silicon-based photodetectors ( $0.8$  A  $W^{-1}$ ).<sup>[40]</sup> Such a high  $R$ -value is attributed to the rationally designed band structure, high carrier mobility, strong co-adsorption ability, and the current amplification by photogating effect. Photogain ( $G$ ) is important to evaluate the performance of a photodetector, which represents the number of photogenerated carriers induced by per incident photon. The  $G$  value can be evaluated using the formula of  $G = I_{ph} \cdot h \cdot \nu / P_{light} \cdot e = R \cdot h \cdot c / e \cdot \lambda$ . Here, the  $\nu$  denotes the frequency of incident light.<sup>[26]</sup> According to the calculated  $R$  values, the  $G$  of our device reaches  $51.3$ , which is two orders of magnitude higher than the reported BP/MoS<sub>2</sub>,<sup>[41]</sup> WSe<sub>2</sub>/MoS<sub>2</sub>,<sup>[42]</sup> and MoTe<sub>2</sub>/MoS<sub>2</sub><sup>[43]</sup> heterojunction photodetector. Thus, the photogenerated carriers can circulate multiple times in the circuit before recombination, which also confirms the presence of photogating effect. In addition to  $R$  and  $G$ , the specific detectivity ( $D^*$ ) is also an important figure-of-merits to evaluate the ability of a photodetector to detect weak signals. The  $D^*$  value can be defined by the equation of  $D^* = (SB)^{1/2} / NEP$  and  $NEP = \bar{i}_n^{2/2} / R$ . Where  $B$  represents the bandwidth, NEP represents the noise equivalent power, and the  $\bar{i}_n^{2/2}$  represents the root mean square of the noise current value.<sup>[30]</sup> To determine the  $D^*$  value, we measured the spectra of current noise power density ( $\bar{i}_n^2$ ) at  $V_{th}^1$  and  $V_{th}^2$  with a fixed  $V_{ds}$  of  $-2$  V (Figure S17a, Supporting Information). The noise spectra display a clear  $1/f$ -noise component in both conditions, while the noise current at  $-60$  V is much lower than that of at  $20$  V due to its lower dark current. Note that the  $1/f$  noise results from random fluctuations of the local electronic state affected by material surface defects and nonuniformity, which are prevalent in all detectors. Here, the noise level per unit bandwidth (1 Hz) is measured to be  $1.3 \times 10^{-27}$  and  $2.7 \times 10^{-25}$  A<sup>2</sup> Hz<sup>-1</sup> at  $V_{gs} = -60$  and  $20$  V, respectively. Meanwhile, the  $D^*$  values under different power densities are summarized in Figure S17b, Supporting Information, which has the maximum  $D^*$  value of  $2.9 \times 10^{14}$  and  $1.2 \times 10^{10}$  Jones at  $V_{gs} = -60$  and  $20$  V, respectively. The obtained  $D^*$  values are comparable to those of commercial silicon-based photodetectors.<sup>[40]</sup> Apart from that, photoswitching stability and response speed are also important parameters for a practical photodetector. In Figure 5c, we demonstrated the photoswitching response of the device at  $V_{gs} = 20$  V and  $V_{ds} = -2$  V, in which 750 periodical on/off laser cycles are applied. The device current quickly increases when the laser turns on and decays to a dark state when turns off. From the ON- and OFF-current of the device, we can conclude that our photodetector has an excellent stability under multiple and repeatable photoswitching, demonstrating its promise for practical applications. Next, we focus on exploring the response speed of the device. In Figure 5d inset, the time-dependent photoresponse measured by a digital oscilloscope is demonstrated. The rise time ( $\tau_{rise}$ ) and decay time ( $\tau_{decay}$ ) of the device are measured as  $130$  and  $260$   $\mu$ s, respectively. Here, the rise (decay) time here defines the time for the device current to increase (decrease) from 10% to 90% (from 90% to 10%) of

the maximum value.<sup>[30]</sup> Meanwhile, the temporal response bandwidth of the device is also evaluated with 3 dB bandwidth, which represents a frequency limit where the light-induced photocurrent is reduced to 0.707-times maximum value. By using a modulated 532 nm pulse laser, our device shows a high 3 dB cutoff frequency of 3 KHz (Figure 5d). These results are comparable to most 2D heterojunction detectors (Figure 4c), which can be attributed the type-II heterojunction combined with a large reverse bias voltage that allows efficient and fast photo-generated carrier separation. The broadband detection is an important advantage for the commercial application of photodetectors. In addition to the above 532 nm laser, our device is capable of fast response for shorter or longer wavelengths (from UV to NIR) as shown in Figure 5e. Here, the incident power density at all wavelengths is controlled at  $3.6$  W  $cm^{-2}$ . In the UV region, both narrow-bandgap BP and large-bandgap MoS<sub>2</sub> have strong light absorption, thus the device has the highest  $I_{light}/I_{dark}$  value of  $1.0 \times 10^3$  at 375 nm (Figure S18, Supporting Information). While in the NIR region, the value is relatively low due to the smaller photon energy of NIR light and the weak absorption of the MoS<sub>2</sub>.

Self-powered photodetectors are highly attractive for low energy-consumption and system simplification because they can operate at zero bias without any external power source and interconnecting wires. Our f-BP/MoS<sub>2</sub> heterojunction photodetector with a type-II energy band alignment is capable of possessing a strong PV effect for self-powered operation. From the photoresponse  $I_{ds} - V_{ds}$  curves (Figure 5a), the  $P_{light}$ -dependent  $V_{oc}$  and  $I_{sc}$  are extracted in Figure S19a, Supporting Information, in which the maximum  $V_{oc}$  and  $I_{sc}$  can achieve  $0.28$  V and  $4.4 \times 10^{-7}$  A, respectively. The high  $V_{oc}$  and  $I_{sc}$  values give our device the ability to perform a perfect self-powered detection. Meanwhile, the  $P_{light}$ -dependent EQE values are calculated as shown in Figure S19b, Supporting Information, where our device exhibits a maximum value of 7.6% at  $P_{light} = 3.1$  mW  $cm^{-2}$ . To verify the sensitivity of the device in self-powered state, we measured the photoswitching response with various  $P_{light}$  from  $0.5$  to  $3600$  mW  $cm^{-2}$  at  $V_{ds} = 0$  V (Figure 5f). Notice that the dark current of the device is stably kept at an ultra-low value of  $3 \times 10^{-13}$  A due to the zero bias. Under light, even with a small power density of  $0.5$  mW  $cm^{-2}$ , the device still has a current boost of three orders of magnitude. As the  $P_{light}$  increases from  $0.5$  to  $3600$  mW  $cm^{-2}$ , the light current increases steadily until a maximum value of  $3.3 \times 10^{-7}$  A, leading to a highest switching ratio of  $1.1 \times 10^6$  (Figure S20, Supporting Information). This switching ratio is two and four orders of magnitude greater than reported MoS<sub>2</sub>/BP<sup>[41]</sup> and MoS<sub>2</sub>/WSe<sub>2</sub><sup>[42]</sup> self-powered photodetectors, indicating its potential application in low energy-consumption optoelectronics.

Considering the anisotropic optical properties of BP layer, it is worth to further investigating the NIR polarization-resolving performances of the device. The test results are shown in Figure 5g. Specifically, when we change the  $\theta$  from  $0^\circ$  to  $360^\circ$ , the device can exhibit a varying photocurrent at different angles while maintaining a fast response. The photocurrent extracted from different angles is further corroborated by the polar plot (Figure 5h). Here, the  $180$ – $360^\circ$  data are replicated from  $0$  to  $180$  degrees due to the repeated tests. We can observe an “8” shape of photocurrent changing with the angle, demonstrating that the device has perfect full-angle polarization detection. Additionally, wavelength-independent polarization ratio is evaluated. As the wavelength

increases from UV to NIR, the polarization ratio of our device increases sequentially, and reaches its highest polarization ratio of 6.98 at 1064 nm (Figure 5i). The reason for this may be that the isotropic MoS<sub>2</sub> also contributes to the photocurrent at UV region and thus diminishes the overall polarization ratio. Our polarization-resolved self-powered photodetector can replace the side-by-side integration of polarized optics and multiple devices and simplify the structure of polarized optoelectronic systems, which has great promise in many professional applications, including astronomy, polarization division multiplexing, and space remote sensing.

## 2.5. Performance Comparison of the Multifunctional Heterojunction

In addition to function switching, the performances of the device are significantly enhanced by the designed photogating mechanism, which is comparable to most previously reported 2D mono-function optoelectronic memories and detectors.<sup>[32,34–37,39,40,43–67]</sup> Figure 4a shows a comprehensive comparison of retention time and multi-bit storage states with other mono-function 2D heterojunction optoelectronic memories, where our device in memory model exhibits an ultra-long retention and a record number of multi-bit storage states. In Figure 4b, we also demonstrate the comparison of maximum programming/erasing ratio (light on/off ratio) and photoresponse wavelength range. Here, both the on/off ratio and photoresponse range are already better than those reported in the past. For the photodetector model, the device performances are also compared with other 2D heterojunction-based photodetectors. Figure 4c exhibits a comprehensive comparison of responsivity and response speed, in which our device can achieve the best balance of response speed and responsivity, especially the responsivity, which is much higher than commercial silicon-based detectors.<sup>[40]</sup> Additionally, considering the polarization-resolved capability of our device, a comparison of the maximum polarization ratio and photoresponse wavelength range is shown in Figure 4d. Benefiting from the photocurrent amplification of photogating effect and anisotropic narrow band-gap BP, our device can obtain an ultra-high polarization ratio while having a good broadband photoresponse. All these results show that our rationally designed heterojunction can not only perform multifunctional operations but also maintain high performance in each function.

## 3. Conclusion

In summary, we have demonstrated that the functionalized-BP/MoS<sub>2</sub> heterojunction can be a multifunction device with gate-controlled free switching of optoelectronic memory and detector. The defect-engineering-induced artificial traps result in a gate-modulated photogating effect, which not only enables function switching but further improves the optoelectronic performances of the device. In the memory model, our device can obtain a speculative storage time of 10 years, an ultra-low dark current of 0.13 pA, an ultra-high on/off ratio of  $3.5 \times 10^7$ , as well as an outstanding multi-bit storage (90 states). In the photodetector model, the device still has an ultrafast response of 130/260 μs, an impressive

responsivity of 22.2 A W<sup>-1</sup>, a stable self-driven broadband detection, and a high polarization ratio of 6.98. All the performances are superior to most previously reported 2D mono-function optoelectronic memories and detectors. We believe that our presented defect-engineering can realize the combination of high performance and multifunction in 2D heterojunction, which can provide a valuable direction for future optoelectronics integration.

## 4. Experimental Section

**Device Fabrication:** The few-layer BP flakes were obtained by mechanical exfoliation from a bulk crystal, and then transferred to a polydimethylsiloxane (PDMS) film. Next, these BP flakes were first oxidized by using ozone to form a bottom self-assembly PO<sub>x</sub> layer. The ozone was produced by UV light in atmospheric conditions. The UV light power density and operating temperature are 53.5 mW cm<sup>-2</sup> and 100 °C, respectively, and the treatment time was set to 60 s. After this, these BP flakes were again transferred to a clean SiO<sub>2</sub> (300 nm)/P<sup>+</sup>-Si substrate by heating the PDMS film at 80 °C for release. Next, the electrode on the BP side was first patterned by a standard electron beam lithography process, and Cr/Au (10/50 nm) electrode was formed by thermal evaporation and a standard lift-off process. After that, the BP flake containing unilateral electrodes was again treated with ozone for 60 s to form a top self-assembly PO<sub>x</sub> layer. Subsequently, few-layer MoS<sub>2</sub> flakes were obtained by the mechanical exfoliation, and then transferred onto the pre-treated BP flake to form f-BP/MoS<sub>2</sub> heterojunction. Here, the transfer process was operated on an aligned transfer platform employing PDMS film as a carrier. Finally, the Cr/Au electrode on the MoS<sub>2</sub> side was formed using the same steps as above.

**Characterization and Measurements:** Raman and PL spectrums were obtained by using a confocal Raman system (Horiba LabRAM HR). The AFM images were obtained by an atomic force microscope (Bioscope system, Bruker). The high-angle annular dark-field STEM images and element mapping analyses were recorded by a Thermo Scientific Themis Z (3.2) microscope equipped with a probe-forming aberration corrector at an operating voltage of 300 kV (Analytical Instrumentation Center of Hunan University). Electrical and photoelectrical measurements were performed on a probe station (Lakeshore, TTP4) using Keysight B1500A and Agilent B2912A semiconductor parameter analyzer under vacuum conditions ( $\approx 8.5 \times 10^{-5}$  Pa). The single-wavelength laser used in photoelectrical measurements includes 375, 457, 532, 660, 808, 914, 1064, and 1550 nm.

**First-Principles Calculation:** The calculation was performed by the open-source QUANTUM ESPRESSO plane-wave DFT package.<sup>[68,69]</sup> The Perdew–Burke–Ernzerhof exchange-correlation functional corrected by the semi-empirical DFT-D3 method was adopted and the plane-wave cut-off energy was 43 Ry.<sup>[70]</sup> Considering the computation burden, the simulated phosphorus consists of 5 layers of 3 × 3 phosphorene with surface oxidation, and a vacuum space of 15 Å was added in the thickness direction to avoid image interactions.<sup>[71]</sup> Moreover, the dipole-correction in this direction was adopted to accurately capture the interlayer charge transfer. The Brillouin zone *k*-point sampling was 2 × 2 × 1 for electronic ground-state computations. Before the band calculation, the oxidized surface was fully relaxed until the force on each atom and total energy variations were smaller than 1 × 10<sup>-4</sup> Ry Bohr<sup>-1</sup> and 1 × 10<sup>-4</sup> Ry.<sup>[72]</sup>

## Supporting Information

Supporting Information is available from the Wiley Online Library or from the author.

## Acknowledgements

This work was supported by the National Key Research and Development Program of Ministry of Science and Technology (No. 2018YFA0703700), China National Funds for Distinguished Young Scientists Grant 61925403,

China National Funds for Outstanding Young Scientists Grant 62122024, the National Natural Science Foundation of China (Grant Nos. 61851403, 12174094, 51872084), Natural Science Foundation of Hunan Province (Grant Nos. 2021JJ20028, 2020JJ1002), Key Research and Development Plan of Hunan Province (Grant Nos. 2022WK2001, 2018GK2064), and Postgraduate Research Innovation Project of Hunan Province (Grant Nos. QL20210114).

## Conflict of Interest

The authors declare no conflict of interest.

## Data Availability Statement

The data that support the findings of this study are available from the corresponding author upon reasonable request.

## Keywords

2D materials, heterojunctions, multifunction devices, optoelectronic memory, photodetectors

Received: June 29, 2022

Revised: August 16, 2022

Published online: November 3, 2022

- [1] R. Cheng, F. Wang, L. Yin, Z. Wang, Y. Wen, T. A. Shifa, J. He, *Nat. Electron.* **2018**, *1*, 356.
- [2] M. Huang, S. Li, Z. Zhang, X. Xiong, X. Li, Y. Wu, *Nat. Nanotechnol.* **2017**, *12*, 1148.
- [3] J. Han, M. He, M. Yang, Q. Han, F. Wang, F. Zhong, M. Xu, Q. Li, H. Zhu, C. Shan, W. Hu, X. Chen, X. Wang, J. Gou, Z. Wu, J. Wang, *Light: Sci. Appl.* **2020**, *9*, 167.
- [4] X. Xiong, J. Kang, Q. Hu, C. Gu, T. Gao, X. Li, Y. Wu, *Adv. Funct. Mater.* **2020**, *30*, 1909645.
- [5] S. Lee, R. Peng, C. Wu, M. Li, *Nat. Commun.* **2022**, *13*, 1485.
- [6] F. Zhou, Z. Zhou, J. Chen, T. H. Choy, J. Wang, N. Zhang, Z. Lin, S. Yu, J. Kang, H. P. Wong, Y. Chai, *Nat. Nanotechnol.* **2019**, *14*, 776.
- [7] Y. An, Y. Hou, K. Wang, S. Gong, C. Ma, C. Zhao, T. Wang, Z. Jiao, H. Wang, R. Wu, *Adv. Funct. Mater.* **2020**, *30*, 2002939.
- [8] H. Wu, Y. Cui, J. Xu, Z. Yan, Z. Xie, Y. Hu, S. Zhu, *Nano Lett.* **2022**, *22*, 2328.
- [9] C. H. Lee, G. H. Lee, A. M. van der Zande, W. Chen, Y. Li, M. Han, X. Cui, G. Arefe, C. Nuckolls, T. F. Heinz, J. Guo, J. Hone, P. Kim, *Nat. Nanotechnol.* **2014**, *9*, 676.
- [10] W. Dang, B. Zhao, C. Liu, X. Yang, L. Kong, Z. Lu, B. Li, J. Li, H. Zhang, W. Li, S. Shi, Z. Qin, L. Liao, X. Duan, Y. Liu, *Nano Res.* **2022**, *15*, 1603.
- [11] Y. Fang, Y. Ge, C. Wang, H. Zhang, *Laser Photonics Rev.* **2020**, *14*, 1900098.
- [12] J. Han, F. Wang, S. Han, W. Deng, X. Du, H. Yu, J. Gou, Q. J. Wang, J. Wang, *Adv. Funct. Mater.* **2022**, *32*, 2205150.
- [13] X. Li, H. Liu, C. Ke, W. Tang, M. Liu, F. Huang, Y. Wu, Z. Wu, J. Kang, *Laser Photonics Rev.* **2021**, *15*, 2100322.
- [14] J. Wang, R. Jia, Q. Huang, C. Pan, J. Zhu, H. Wang, C. Chen, Y. Zhang, Y. Yang, H. Song, F. Miao, R. Huang, *Sci. Rep.* **2018**, *8*, 17755.
- [15] W. Zhu, X. Wei, F. Yan, Q. Lv, C. Hu, K. Wang, *J. Semicond.* **2019**, *40*, 092001.
- [16] X. Zhou, X. Hu, S. Zhou, H. Song, Q. Zhang, L. Pi, L. Li, H. Li, J. Lu, T. Zhai, *Adv. Mater.* **2018**, *30*, 1703286.
- [17] C. Liu, X. Zou, M. C. Wu, Y. Wang, Y. Lv, X. Duan, S. Zhang, X. Liu, W. W. Wu, W. Hu, Z. Fan, L. Liao, *Adv. Funct. Mater.* **2021**, *31*, 2100781.
- [18] N. Huo, G. Konstantatos, *Adv. Mater.* **2018**, *30*, 1801164.
- [19] T. Ahmed, S. Kuriakose, S. Abbas, M. J. S. Spencer, M. A. Rahman, M. Tahir, Y. Lu, P. Sonar, V. Bansal, M. Bhaskaran, S. Sriram, S. Walia, *Adv. Funct. Mater.* **2019**, *29*, 1901991.
- [20] S. Ippolito, P. Samori, *Small Sci.* **2022**, *2*, 2100122.
- [21] Q. Liang, Q. Zhang, X. Zhao, M. Liu, A. T. S. Wee, *ACS Nano* **2021**, *15*, 2165.
- [22] Z. Lin, B. R. Carvalho, E. Kahn, R. Lv, R. Rao, H. Terrones, M. A. Pimenta, M. Terrones, *2D Mater.* **2016**, *3*, 022002.
- [23] G. Lee, S. J. Pearton, F. Ren, J. Kim, *ACS Appl. Mater. Interfaces* **2018**, *10*, 10347.
- [24] X. Jiang, X. Shi, M. Zhang, Y. Wang, Z. Gu, L. Chen, H. Zhu, K. Zhang, Q. Sun, D. W. Zhang, *ACS Appl. Nano Mater.* **2019**, *2*, 5674.
- [25] X. Zong, H. Hu, G. Ouyang, J. Wang, R. Shi, L. Zhang, Q. Zeng, C. Zhu, S. Chen, C. Cheng, B. Wang, H. Zhang, Z. Liu, W. Huang, T. Wang, L. Wang, X. Chen, *Light: Sci. Appl.* **2020**, *9*, 114.
- [26] L. Wang, X. Zou, J. Lin, J. Jiang, Y. Liu, X. Liu, X. Zhao, Y. F. Liu, J. C. Ho, L. Liao, *ACS Nano* **2019**, *13*, 4804.
- [27] J. Bullock, M. Amani, J. Cho, Y.-Z. Chen, G. H. Ahn, V. Adinolfi, V. R. Shrestha, Y. Gao, K. B. Crozier, Y.-L. Chueh, A. Javey, *Nat. Photonics* **2018**, *12*, 601.
- [28] H. Yuan, X. Liu, F. Afshinmanesh, W. Li, G. Xu, J. Sun, B. Lian, A. G. Curto, G. Ye, Y. Hikita, Z. Shen, S. C. Zhang, X. Chen, M. Brongersma, H. Y. Hwang, Y. Cui, *Nat. Nanotechnol.* **2015**, *10*, 707.
- [29] L. Huang, N. Huo, Y. Li, H. Chen, J. Yang, Z. Wei, J. Li, S. S. Li, *J. Phys. Chem. Lett.* **2015**, *6*, 2483.
- [30] M. Long, P. Wang, H. Fang, W. Hu, *Adv. Funct. Mater.* **2018**, *29*, 1803807.
- [31] S. Wei, F. Wang, X. Zou, L. Wang, C. Liu, X. Liu, W. Hu, Z. Fan, J. C. Ho, L. Liao, *Adv. Mater.* **2019**, *32*, 1907527.
- [32] D. Xiang, T. Liu, J. Xu, J. Y. Tan, Z. Hu, B. Lei, Y. Zheng, J. Wu, A. H. C. Neto, L. Liu, W. Chen, *Nat. Commun.* **2018**, *9*, 2966.
- [33] F. Guo, B. Yang, Y. Yuan, Z. Xiao, Q. Dong, Y. Bi, J. Huang, *Nat. Nanotechnol.* **2012**, *7*, 798.
- [34] J. Lee, S. Pak, Y. W. Lee, Y. Cho, J. Hong, P. Giraud, H. S. Shin, S. M. Morris, J. I. Sohn, S. Cha, J. M. Kim, *Nat. Commun.* **2017**, *8*, 14734.
- [35] D. Lee, E. Hwang, Y. Lee, Y. Choi, J. S. Kim, S. Lee, J. H. Cho, *Adv. Mater.* **2016**, *28*, 9196.
- [36] J. Zhao, Z. Wei, X. Yang, G. Zhang, Z. Wang, *Nano Energy* **2021**, *82*, 105692.
- [37] M. D. Tran, H. Kim, J. S. Kim, M. H. Doan, T. K. Chau, Q. A. Vu, J. H. Kim, Y. H. Lee, *Adv. Mater.* **2019**, *31*, 1807075.
- [38] J. Y. Chen, Y. C. Chiu, Y. T. Li, C. C. Chueh, W. C. Chen, *Adv. Mater.* **2017**, *29*, 1702217.
- [39] Q. Wang, Y. Wen, K. Cai, R. Cheng, L. Yin, Y. Zhang, J. Li, Z. Wang, F. Wang, F. Wang, T. A. Shifa, C. Jiang, H. Yang, J. He, *Sci. Adv.* **2018**, *4*, eaap7916.
- [40] X. Wang, Z. Cheng, K. Xu, H. K. Tsang, J.-B. Xu, *Nat. Photonics* **2013**, *7*, 888.
- [41] T. Hong, B. Chamlagain, T. Wang, H.-J. Chuang, Z. Zhou, Y.-Q. Xu, *Nanoscale* **2015**, *7*, 18537.
- [42] H. S. Lee, J. Ahn, W. Shim, S. Im, D. K. Hwang, *Appl. Phys. Lett.* **2018**, *113*, 163102.
- [43] A. Pezeshki, S. H. H. Shokouh, T. Nazari, K. Oh, S. Im, *Adv. Mater.* **2016**, *28*, 3216.
- [44] F. Gao, X. Zhang, B. Tan, S. Zhang, J. Zhang, D. Jia, Y. Zhou, P. Hu, *Small* **2021**, *17*, 2104459.
- [45] W. Huang, L. Yin, F. Wang, R. Cheng, Z. Wang, M. G. Sendeku, J. Wang, N. Li, Y. Yao, X. Yang, C. Shan, T. Yang, J. He, *Adv. Funct. Mater.* **2019**, *29*, 1902890.
- [46] Z. Yang, H. Hong, F. Liu, Y. Liu, M. Su, H. Huang, K. Liu, X. Liang, W. J. Yu, Q. A. Vu, X. Liu, L. Liao, *Small* **2019**, *15*, e1804661.
- [47] Y. Zhai, X. Yang, F. Wang, Z. Li, G. Ding, Z. Qiu, Y. Wang, Y. Zhou, S. T. Han, *Adv. Mater.* **2018**, *30*, 1803563.



- [48] F. Li, B. Xu, W. Yang, Z. Qi, C. Ma, Y. Wang, X. Zhang, Z. Luo, D. Liang, D. Li, Z. Li, A. Pan, *Nano Res.* **2020**, *13*, 1053.
- [49] X. Zhai, X. Xu, J. Peng, F. Jing, Q. Zhang, H. Liu, Z. Hu, *ACS Appl. Mater. Interfaces* **2020**, *12*, 24093.
- [50] T. Yang, X. Li, L. Wang, Y. Liu, K. Chen, X. Yang, L. Liao, L. Dong, C.-X. Shan, *J. Mater. Sci.* **2019**, *54*, 14742.
- [51] F. Wang, L. Yin, Z. X. Wang, K. Xu, F. M. Wang, T. A. Shifa, Y. Huang, C. Jiang, J. He, *Adv. Funct. Mater.* **2016**, *26*, 5499.
- [52] J. Tan, H. Nan, Q. Fu, X. Zhang, X. Liu, Z. Ni, K. Ostrikov, S. Xiao, X. Gu, *Adv. Electron. Mater.* **2021**, *8*, 2100673.
- [53] Z. Zhang, B. Zhao, D. Shen, Q. Tao, B. Li, R. Wu, B. Li, X. Yang, J. Li, R. Song, H. Zhang, Z. Huang, Z. Zhang, J. Zhou, Y. Liu, X. Duan, *Small Struct.* **2021**, *2*, 2100028.
- [54] H. Henck, D. Pierucci, J. Chaste, C. H. Naylor, J. Avila, A. Balan, M. G. Silly, M. C. Asensio, F. Sirotti, A. T. C. Johnson, E. Lhuillier, A. Ouerghi, *Appl. Phys. Lett.* **2016**, *109*, 113103.
- [55] H. Xu, J. Wu, Q. Feng, N. Mao, C. Wang, J. Zhang, *Small* **2014**, *10*, 2300.
- [56] C. Ma, Y. Shi, W. Hu, M. H. Chiu, Z. Liu, A. Bera, F. Li, H. Wang, L. J. Li, T. Wu, *Adv. Mater.* **2016**, *28*, 3683.
- [57] Z. Xu, S. Lin, X. Li, S. Zhang, Z. Wu, W. Xu, Y. Lu, S. Xu, *Nano Energy* **2016**, *23*, 89.
- [58] P. L. Chen, Y. Chen, T. Y. Chang, W. Q. Li, J. X. Li, S. Lee, Z. Fang, M. Li, A. Majumdar, C. H. Liu, *ACS Appl. Mater. Interfaces* **2022**, *14*, 24856.
- [59] D. Wu, M. Xu, L. Zeng, Z. Shi, Y. Tian, X. J. Li, C.-X. Shan, J. Jie, *ACS Nano* **2022**, *16*, 5545.
- [60] S. Zhao, J. Wu, K. Jin, H. Ding, T. Li, C. Wu, N. Pan, X. Wang, *Adv. Funct. Mater.* **2018**, *28*, 1802011.
- [61] J. Ahn, J.-H. Kyhm, H. K. Kang, N. Kwon, H.-K. Kim, S. Park, D. K. Hwang, *ACS Photonics* **2021**, *8*, 2650.
- [62] J. Ahn, K. Ko, J.-H. Kyhm, H.-S. Ra, H. Bae, S. Hong, D.-Y. Kim, J. Jang, T. W. Kim, S. Choi, J.-H. Kang, N. Kwon, S. Park, B.-K. Ju, T.-C. Poon, M.-C. Park, S. Im, D. K. Hwang, *ACS Nano* **2021**, *15*, 17917.
- [63] Y. Xin, X. Wang, Z. Chen, D. Weller, Y. Wang, L. Shi, X. Ma, C. Ding, W. Li, S. Guo, R. Liu, *ACS Appl. Mater. Interfaces* **2020**, *12*, 15406.
- [64] T. Y. Chang, P. L. Chen, J. H. Yan, W. Q. Li, Y. Y. Zhang, D. I. Luo, J. X. Li, K. P. Huang, C. H. Liu, *ACS Appl. Mater. Interfaces* **2020**, *12*, 1201.
- [65] L. H. Zeng, Q. M. Chen, Z. X. Zhang, D. Wu, H. Yuan, Y. Y. Li, W. Qarony, S. P. Lau, L. B. Luo, Y. H. Tsang, *Adv. Sci.* **2019**, *6*, 1901134.
- [66] D. Liu, J. Hong, X. Wang, X. Li, Q. Feng, C. Tan, T. Zhai, F. Ding, H. Peng, H. Xu, *Adv. Funct. Mater.* **2018**, *28*, 1804696.
- [67] Y. Niu, R. Frisenda, E. Flores, J. R. Ares, W. Jiao, D. Perez de Lara, C. Sánchez, R. Wang, I. J. Ferrer, A. Castellanos-Gomez, *Adv. Opt. Mater.* **2018**, *6*, 1800351.
- [68] P. Giannozzi, S. Baroni, N. Bonini, M. Calandra, R. Car, C. Cavazzoni, D. Ceresoli, G. L. Chiarotti, M. Cococcioni, I. Dabo, A. Dal Corso, S. de Gironcoli, S. Fabris, G. Fratesi, R. Gebauer, U. Gerstmann, C. Gougoussis, A. Kokalj, M. Lazzeri, L. Martin-Samos, N. Marzari, F. Mauri, R. Mazzarello, S. Paolini, A. Pasquarello, L. Paulatto, C. Sbraccia, S. Scandolo, G. Sclauzero, A. P. Seitsonen, et al., *J. Phys.: Condens. Matter* **2009**, *21*, 395502.
- [69] P. Giannozzi, O. Andreussi, T. Brumme, O. Bunau, M. Buongiorno Nardelli, M. Calandra, R. Car, C. Cavazzoni, D. Ceresoli, M. Cococcioni, N. Colonna, I. Carnimeo, A. Dal Corso, S. de Gironcoli, P. Delugas, R. A. DiStasio, A. Ferretti, A. Floris, G. Fratesi, G. Fugallo, R. Gebauer, U. Gerstmann, F. Giustino, T. Gorni, J. Jia, M. Kawamura, H. Y. Ko, A. Kokalj, E. Küçükbenli, M. Lazzeri, et al., *J. Phys.: Condens. Matter* **2017**, *29*, 465901.
- [70] V. Shukla, R. L. Kumawat, N. K. Jena, B. Pathak, R. Ahuja, *ACS Appl. Electron. Mater.* **2021**, *3*, 733.
- [71] H. Liu, A. T. Neal, Z. Zhu, Z. Luo, X. Xu, D. Tománek, P. D. Ye, *ACS Nano* **2014**, *8*, 4033.
- [72] A. Ziletti, A. Carvalho, D. K. Campbell, D. F. Coker, A. H. Castro Neto, *Phys. Rev. Lett.* **2015**, *114*, 046801.